IOP Publishing Plasma Sources Science and Technology

Plasma Sources Sci. Technol. **24** (2015) 065015 (9pp) doi:10.1088/0963-0252/24/6/065015

Complex image method for RF antenna-plasma inductive coupling calculation in planar geometry. Part II: measurements on a resonant network

Ph Guittienne[1], R Jacquier[2], A A Howling[2] and I Furno[2]

[1] Helyssen, Route de la Louche 31, CH-1092 Belmont-sur-Lausanne, Switzerland
[2] Ecole Polytechnique Fédérale de Lausanne (EPFL), Swiss Plasma Center, CH-1015 Lausanne, Switzerland

E-mail: alan.howling@epfl.ch

Received 2 June 2015, revised 24 September 2015
Accepted for publication 19 October 2015
Published 6 November 2015

Abstract

Measurements and analysis of a radio-frequency planar antenna are presented for applications in inductively-coupled plasma processing. The network of inductive and capacitive elements exhibits high currents under resonance which are efficient for plasma generation. Mode frequencies and impedances are accurately calculated by accounting for the mutual partial inductances using the impedance matrix. The effect of plasma inductive coupling on mode frequency shift and mode impedance is estimated using the complex image method, giving good agreement with experiment. It is proposed that the complex image method combined with the partial inductance concept (see the accompanying paper, Part I (Howling *et al* 2015 *Plasma Sources Sci. Technol.* **24** 065014)) offers a general way to calculate the impedance characteristics of inductively-coupled plasma sources in planar geometry.

Keywords: inductively-coupled plasma, complex image method, partial inductance, RF antenna

(Some figures may appear in colour only in the online journal)

1. Introduction

This paper is the second part of the complex image method for inductively-coupled plasma. Part I [1] showed how the mutual inductance between a conductor and a plasma can be described by an image current at a complex depth in the plasma; this second part applies the method to experiments on a planar resonant network antenna. It will be shown how the effects of plasma inductive coupling can be calculated for the complicated geometry of these plasma sources.

When excited at a resonance frequency, a RF resonant network develops very high currents within its structure, which can be used for inductively-coupled plasma (ICP) sources [2–6]. They are good candidates for large area processing, with a particular advantage because of their high and real input impedance. The transition between capacitive and inductive coupling was demonstrated, and measurements of the plasma loading effect on the network impedance showed shifts in the resonant frequencies and a strong decrease in the network Q factor. However, since the network is usually excited by a fixed frequency RF generator, the question of off-resonance excitation naturally arises.

From a theoretical point of view, a lumped element analysis of dissipative resonant networks [7] gave analytical expressions for network impedance and current distribution. However, it fails to correctly predict the mode resonance frequency spectrum. Furthermore, the coupling between network and plasma could only be estimated empirically via an effective leg resistance and inductance. Both of these shortcomings are because the mutual inductances between the network elements [8] and with the plasma were neglected. This is a critical point for source design because the network resonance

spectrum must be accurately matched to the frequency of the RF generator (usually 13.56 MHz). The complex image method in Part I [1] will be used to calculate the plasma coupling in terms of plasma properties.

This paper is organized as follows: After describing the experimental setup in section 2, a matrix model for the antenna impedance is developed using mutual partial inductances in section 3. The complex image method from Part I [1] is used to calculate the mutual inductive coupling between the antenna and the plasma. The matrix model is compared with vacuum measurements of node voltages and antenna input impedance in section 4. Finally, plasma loading measurements for the antenna operating as an ICP source are interpreted using the complex image method in section 5 before concluding.

2. Experimental setup

2.1. The antenna assembly

A schematic of the experimental setup used for this study is shown in figure 1. The network is made of $N = 23$ identical tubular copper legs, overall length 20 cm, radius $a = 0.3$ cm, with parallel axes spaced 2.5 cm apart. Accounting for the current path, the effective leg length is $l_{\text{leg}} = 19.2$ cm. The legs are connected at both ends by stringers which consist of 2.6 nF ceramic capacitor assemblies with copper strip connectors $l_{\text{str}} = 1.9$ cm long and $w = 0.6$ cm wide. In figure 1(b), the antenna assembly is set in an open top metal housing with the axes of the antenna leg network $h_{\text{screen}} = 5.5$ cm above the baseplate screen. The housing is filled with a polyimide foam dielectric to a level 0.6 cm above the leg axes, and the surface is protected by 0.3 cm thick glass. The RF input power is centrally connected at node A12 in figure 1(a), with ground connections at extreme ends A1 and A23 (for modes $m/2$ odd), or B1 and B23 (for modes $m/2$ even) to ensure symmetrical power feeding. The whole system is placed inside a vacuum vessel and connected via 30 cm of 50 Ω cable inside the vacuum vessel (with 4 cm stubs to RF and in parallel to both ground connections) to a vacuum feedthrough.

The antenna is cooled by water flow through the leg tubes. The plasma volume above the antenna is closed by a slotted metal plate 5.5 cm above the glass surface which defines the electrode gap in figure 1(b). The plasma density was mapped using the ion saturated currents measured by an array of 15 Langmuir probes which traverse the antenna length through the slots which are perpendicular to the legs.

The RF characterization of the uncoupled (without plasma) antenna was performed by network analyser measurements of the antenna input impedance spectrum at the vacuum feedthrough, and by measurements of the network node voltages A_n and B_n with high impedance probes. The plasma-coupled network was electrically characterized by measuring its input impedance using a current/voltage/phase probe (Z-Scan™ [9] from Advanced Energy), at the same vacuum feedthrough, as a function of frequency for several modes. The same probe was used to measure the RF power delivered to the antenna.

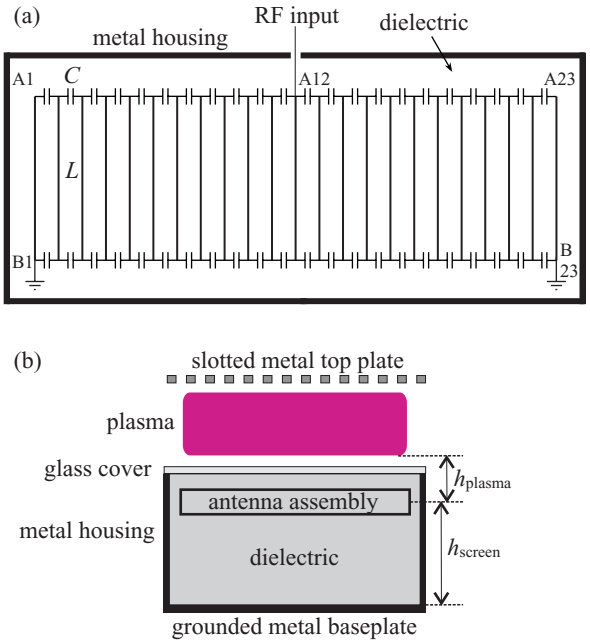

Figure 1. The planar resonant network antenna assembly. (a) Top view, showing one configuration of the electrical connections; (b) side view from one end of the antenna. The antenna is 55 cm long and 20 cm wide. The other dimensions are given in the text.

The experimental parameters were 1 Pa pressure of argon with 50–500 W delivered power at 13.56 MHz for mode $m = 6$ measurements; and also a frequency range from 10 to 23 MHz at 200 W to excite modes $m = 2, 4, 6, 8, 10$.

2.2. The antenna equivalent circuit

The antenna circuit in figure 2 is a balanced high-pass filter ladder network. This lumped element equivalent circuit is a valid approximation because the antenna dimensions are small compared to the wavelength of the RF excitation (22 m in vacuum at 13.56 MHz). The legs have self partial inductance L_{leg} determined by their geometry (see appendix A), with a small resistance R estimated from their skin depth resistance in copper. The high-quality-factor capacitor assemblies C in the stringers have copper strips linking the legs, having self partial inductance L_{str} and resistance r given by the skin depth resistance plus the effective series resistance (ESR) of the capacitor assemblies.

Mutual partial inductance exists between parallel conductors, but not between orthogonal conductors. Therefore each leg has a mutual partial inductance only with the other legs $M^{\text{leg/leg}}$, whereas each stringer has mutual partial inductance with the stringers in the same line $M^{\text{str/line}}$, and also with the stringers on the opposite side of the antenna $M^{\text{str/opp}}$, as indicated in figure 2. This means that one impedance matrix can be defined for the legs, and another independently for the stringers. In this work, all of the inductances are partial inductances, therefore the subscript 'p' for 'partial' in Part I [1] is dropped here in Part II. Expressions for the mutual partial inductances used in this work are given in appendix A.

Throughout this work we consider high-pass networks as a specific example for plasma applications, although other

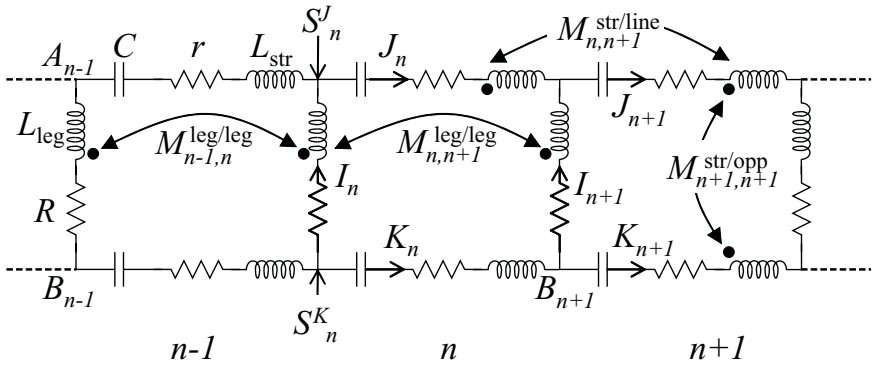

Figure 2. The antenna network of identical meshes $\{..., n-1, n, n+1, ...\}$, showing the leg self partial inductances L_{leg} with resistance R, linked by stringers with capacitors C and short connectors of self partial inductance L_{str} with combined resistance r. The arrows represent coupling by mutual partial inductances. I_n are the leg currents, J_n and K_n are respectively the upper and lower stringer currents. S^J_n and S^K_n are the source currents, and A_n and B_n the voltages, at the upper and lower nodes, respectively. Only a few representative labels are shown for clarity.

resonant antenna configurations can also be envisaged (low-pass, hybrid, etc).

3. Matrix of partial inductances for plasma source network analysis

In contrast to previous analyses of the planar resonant antenna [2, 7], the mutual partial inductances between all elements, including the metal baseplate and the plasma, are accounted for in this section. The resulting impedance matrix is used to calculate the input impedance of the antenna, and the distribution of currents and voltages for any symmetrical arrangement of RF power feeding and ground connections.

The values of the resistances and capacitances are independent of their position in the circuit of figure 2, whereas the net partial inductances of the legs and the stringers depend on their location in the network. This is because their inductive coupling is different according to the number, position and currents of their neighbours. For example, current I_q in leg q couples a magnetic flux $M^{leg/leg}_{nq} I_q$ with leg n, where $M^{leg/leg}_{nq}$ is their mutual partial inductance which is a purely geometrical quantity [1, 10, 11]. By the principle of superposition, this flux is independent of fields caused by other currents. The current I_q itself may be influenced by the circuit response to coupling with other circuits, but its flux coupled with leg n is always $M^{leg/leg}_{nq} I_q$, independent of fluxes produced elsewhere. The total flux coupled to leg n, due to currents in the legs, is therefore $\sum_{q=1}^{N} M^{leg/leg}_{nq} I_q$. Note that $M^{leg/leg}_{nn} \equiv L_{leg}$ is the self partial inductance of a leg [10, 12]. In previous analytical work [7], all the $M^{leg/leg}_{nq} = 0$ for $n \neq q$.

The combined effect of the inductive coupling of the antenna elements, the baseplate, and the plasma is therefore represented as in figure 3, using the results of Part I [1].

Because the net partial inductance of each element depends on its position $\{1, 2, ...n, ... N\}$ in the network, a matrix will be necessary to define the antenna impedance. An advantage of the partial inductance approach [10, 11] is that the impedance matrix of any network is built up from the mutual partial inductances between pairs of elements, which are easily calculated.

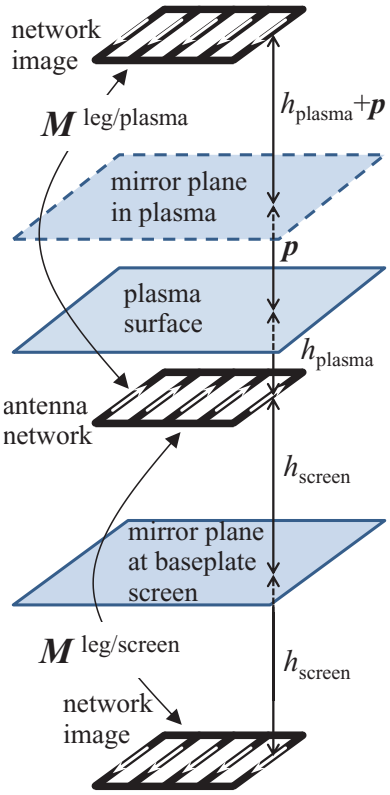

Figure 3. Schematic of mutual inductive coupling for the same configuration of antenna, baseplate, and plasma as in figure 1(b). The network is coupled to its image currents in the baseplate screen, according to the method of images, by their mutual inductance $\mathbf{M}^{leg/screen}$. The network is also coupled to its image currents in the plasma, at a complex distance according to the complex image method (see Part I [1]), by their mutual inductance $\mathbf{M}^{leg/plasma}$. The white arrows represent the currents and image currents of the legs. The stringer couplings are not shown for clarity.

To define the impedance matrices, we first consider Ohm's law for the nth leg, with reference to figures 2 and 3, where currents are taken to be time harmonic. Applying the superposition principle for the screen- and plasma-coupled image currents,

$$B_n - A_n = RI_n + \mathrm{j}\omega \sum_{q=1}^{N} (M_{nq}^{\mathrm{leg/leg}} - M_{nq}^{\mathrm{leg/screen}} - M_{nq}^{\mathrm{leg/plasma}}) I_q, \quad (1)$$

where $\mathrm{j}\omega M_{nq}^{\mathrm{leg/plasma}} I_q$ is the voltage induced in leg n due to the image in the plasma of current I_q in leg q, and similarly for the baseplate.

Equivalently, Ohm's law in (1) can be expressed as a matrix equation for all the N legs using $N \times N$ matrices for the impedances, and column vectors for the voltages and currents:

$$\vec{B} - \vec{A} = \mathbf{R}\vec{I} + \mathrm{j}\omega(\mathbf{M}^{\mathrm{leg/leg}} - \mathbf{M}^{\mathrm{leg/screen}} - \mathbf{M}^{\mathrm{leg/plasma}})\vec{I}, \quad (2)$$

where $\mathbf{R} = R\mathbf{1}$ is the leg resistance multiplied by the $N \times N$ identity matrix, and the mutual partial inductance matrices are given in appendix B. $\mathbf{M}^{\mathrm{leg/plasma}}$ is the mutual partial inductance matrix between the legs and their images in the plasma. The magnitude of mutual inductance decreases with distance, therefore higher order reflections (such as the image in the screen of the antenna image in the plasma) have been considered negligibly weak. Note that the method of images for perfect screens is valid for finite linear current segments, and we assume that this applies also to the complex image method. Experimentally, the influence of the baseplate screen was small but clearly observable, whereas the effect of the top plate (see figure 1(b)) was much smaller because the slots inhibited circulating image currents. Hence the top plate was neglected in the calculations of impedance matrices.

From (2), the impedance matrix of the antenna legs is directly

$$\mathbf{Z}_{\mathrm{leg}} = R\mathbf{1} + \mathrm{j}\omega(\mathbf{M}^{\mathrm{leg/leg}} - \mathbf{M}^{\mathrm{leg/screen}} - \mathbf{M}^{\mathrm{leg/plasma}}). \quad (3)$$

The stringer impedance matrix $\mathbf{Z}_{\mathrm{str}}$ is derived similarly in appendix B.

The required solutions for the antenna electrical properties are found using Kirchoff's laws, similarly to the analytical solution in [7], except that now matrix equations are used because of the mutual inductance terms. The matrix solution is derived in appendix B, where the antenna currents, voltages, and input impedance are determined in terms of the impedance matrices $\mathbf{Z}_{\mathrm{leg}}$ and $\mathbf{Z}_{\mathrm{str}}$, along with the source current vectors $\vec{\mathrm{S}}^{\mathrm{J}}$ and $\vec{\mathrm{S}}^{\mathrm{K}}$. For example, the leg current distribution is given by:

$$\vec{I} = (\mathbf{U}\mathbf{Z}_{\mathrm{str}}^{-1}\mathbf{U}^{T}\mathbf{Z}_{\mathrm{leg}} + 2\mathbf{1})^{-1}(\vec{S}^{K} - \vec{S}^{J}), \quad (4)$$

where the matrix $\mathbf{U}$ is defined in appendix B, and the antenna input impedance is

$$Z_{\mathrm{in}} = A_{\mathrm{RFnode}}/S^{J}_{\mathrm{RFnode}}, \quad (5)$$

where $n =$ 'RFnode' refers to the node of the RF input connection, which was $n = 12$ for all experiments presented here. Although the matrix solution can be written down, the values must be calculated by computer because of the difficulty of matrix inversion. The complex image method thus provides a practical way to calculate inductive plasma coupling of even very complicated antenna networks which would be prohibitively difficult using the transformer model [1, 13, 14]. The results of the plasma coupling model will be compared with experiments in section 5.

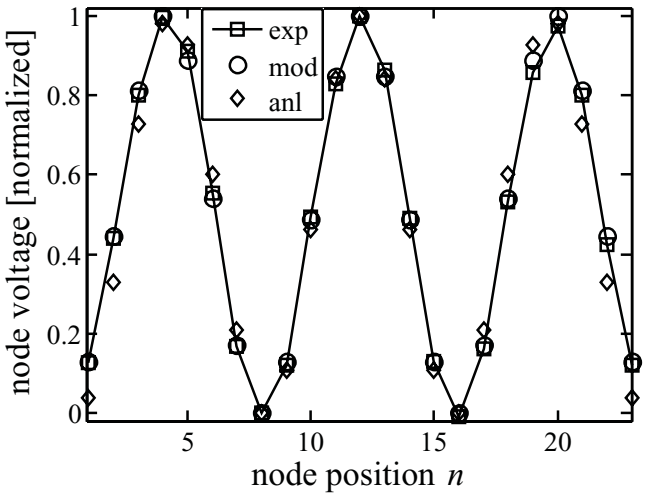

Figure 4. Voltage distribution A_n for a $m = 6$ mode on the 23-leg network. Experimental measurements ('exp') are compared with the matrix model for mutual inductances ('mod'), and with the analytical solution ('anl') calculated using [7]. The RF input was at $n = 12$ and ground connections at $n = 8$ and 16 for this figure.

4. Experimental results and comparison with theory for the antenna in vacuum

The validity of the mutual partial inductance model is first verified by comparison with experiments for the antenna system with baseplate, in vacuum (no plasma).

4.1. Voltage distribution for the network modes

Comparison of voltage node measurements with the mutual inductance solution for antenna voltages shows excellent agreement in figure 4. The solution given by the analytical approach from [7] is not as accurate, but nevertheless shows that the mode structure on the antenna is not strongly perturbed by the mutual inductance between antenna elements and the screen. When the excitation frequency is off resonance, the distortion of the voltage distribution is also reproduced in detail by the mutual inductance matrix model, see figure 5.

4.2. Prediction of the mode frequencies without plasma

The strong effect of mutual inductance is more clearly seen when the measured mode frequencies are compared with the matrix and analytical models in figure 6. The introduction of the mutual inductances is clearly necessary [8] to obtain good agreement with experiment, and this was lacking in previous papers on resonant network antennas [2, 3, 5, 7]. Accounting for the mutual inductances, the impedance spectrum is accurately reproduced for any configuration of the ground return connections. The effect of the mutual inductances is to 'compress' the range of mode frequencies, with the result that

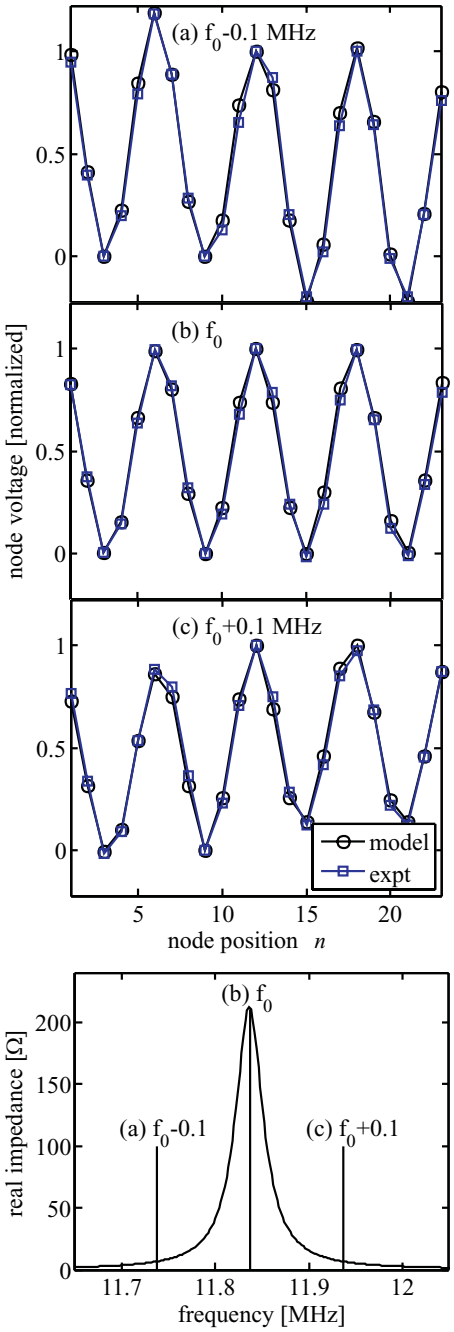

Figure 5. Comparison of measured and matrix-calculated node voltage distributions, A_n, for a $m = 8$ mode (a) below, (b) at, and (c) above resonance frequency $f_0 = 11.84$ MHz in vacuum. RF voltage amplitudes are normalized to the RF input voltage at the central node A_{12}. To exaggerate the voltage asymmetry, only a single ground node connection was used, at node $n = 9$. The corresponding frequencies are shown in the bottom figure relative to the mode impedance measurement near resonance.

the frequencies of intermediate mode numbers $m = 5$, 6 are almost unaffected by the mutual inductive coupling.

This excellent agreement with experimental results lends confidence to the matrix model for mutual inductive coupling between the antenna elements and with the screen. In the following sections, this approach is consequently extended to include plasma inductive coupling, using the plasma-antenna

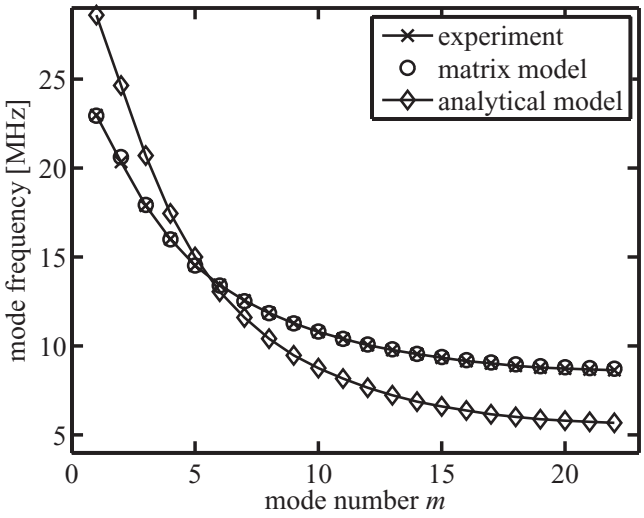

Figure 6. Measurement of the network resonance frequencies (×) compared with the matrix model (○) for mutual inductance, and with an analytical model (◊) [7], all without plasma.

mutual inductance calculated by the complex image method [1].

5. Experimental results and comparison with theory for plasma coupling to the antenna

Figure 7(a) shows the antenna input impedance spectra measured at the vacuum feedthrough for modes $m = 2$, 4, 6, 8, 10 in vacuum and also with plasma. The plasma experiments were carried out using a variable frequency RF generator for a nominal constant delivered power of 200 W. Due to the practical difficulty of maintaining the desired RF delivered power and matching for strongly off-resonance conditions, the plasma measurements were made across each mode resonance for a limited phase range of $-\pi/4$ to $+\pi/4$ radians.

Figure 7(b) shows calculations of the corresponding input impedance mode spectra using the mutual partial inductance matrix model. The calculated impedance values have been transformed through 30 cm of 50 Ω transmission line to compare with the experimental measurements (with 4 cm stubs to RF and in parallel to both ground connections). For the vacuum impedance spectra, the calculations of section 3 are in good agreement with the measured mode frequencies, as already mentioned in section 4.2, and also with the impedance magnitudes and resonance widths. Furthermore, figures 7(a) and (b) also show reasonably good agreement for the frequency shifts and strong reductions in input impedance in the presence of plasma loading of the antenna.

The plasma coupling with the antenna in figure 7(b) was calculated using the complex image model [1] according to section 3. Only the dominant coupling with the leg mutual inductances was considered for the plasma coupling since the stringer coupling is much smaller. Inductive plasma coupling was therefore entirely described by $\mathbf{M}^{\mathrm{leg/plasma}}$, which depends on geometrical dimensions and the complex plasma skin depth $\mathbf{p}$, defined by the electron density and the electron-neutral collision frequency [1], as follows:

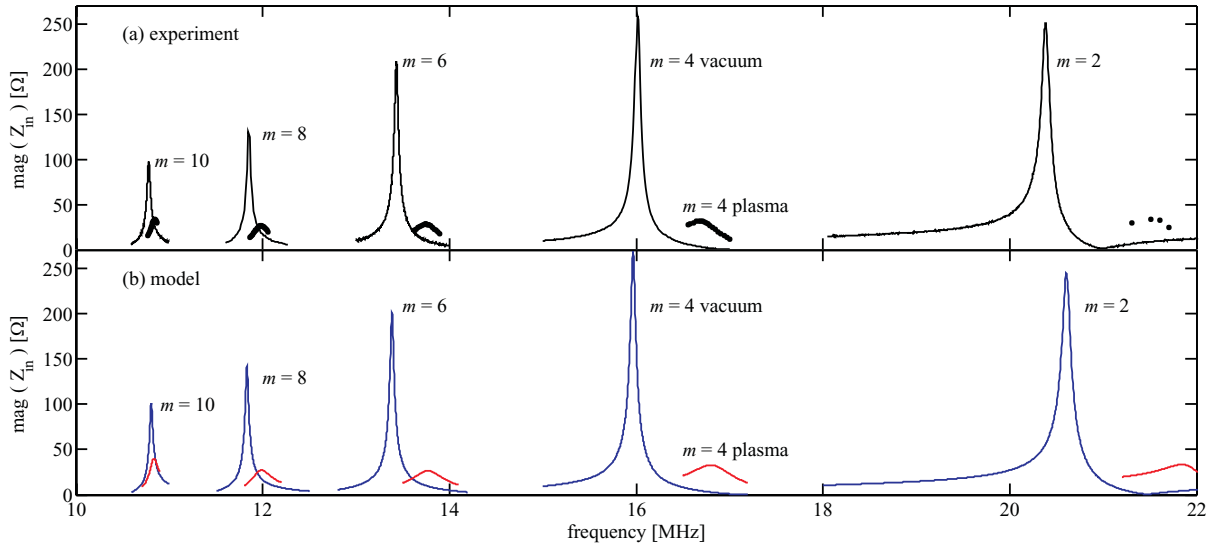

Figure 7. (a) Measurements of the mode impedance spectra in vacuum and with plasma (shown by points). (b) Calculations of the mode impedance spectra using the impedance matrix model. The mutual partial inductance due to plasma coupling with the antenna was estimated using the complex image model [1]. Nominal experimental parameters were argon pressure 1 Pa and 200 W delivered power.

(i) The distance between the antenna leg axes and the plasma/sheath boundary, $h_{\text{plasma}} = 1.2$ cm, was chosen according to 0.9 cm from the leg axes to the glass top surface (figure 1(b)), plus an estimated 0.3 cm for the sheath width (corresponding to about four Debye lengths for the undriven sheath in these plasma conditions [15]).

(ii) The argon pressure determines the electron-neutral collision frequency ν_{m} [rad/s] $\approx 2.6 \cdot 10^7 \cdot p$ [Pa] for typical electron temperature in these plasma conditions [15]. A value of 1.3 Pa, instead of the nominal pressure of 1 Pa, was found to give the best fit and was used for all calculations in this work. Since the RF frequency and pressure were constant in figure 7, the collisionality $\nu_{\text{m}}/\omega \sim 0.4$.

(iii) The line-averaged plasma density was estimated by microwave interferometry [2] to be approximately $3 \cdot 10^{16}$ m^{-3} for 200 W delivered power. The plasma densities for the different modes were then estimated according to the relative ion saturated currents of the Langmuir probes, assuming that the electron temperature remained in a narrow range as could be expected by consideration of particle balance [15]. For $m = \{2, 4, 6, 8, 10\}$, $n_{\text{e}} \approx \{2.3, 3.8, 4.6, 4.6, 3.0\} \cdot 10^{16}$ m^{-3}. These values were used for the model calculations.

The Langmuir probes typically measured a dome profile with approximately a 50% drop in plasma density from the centre to the antenna edges [2]. Using the model, only a very small influence of different profiles of plasma density was found on the frequency shifts and mode impedances. We attribute this to the spatial averaging effect of mutual inductances across all the bars. The typical measured density profile was used for all model calculations in this work.

The mode frequency shifts and the impedance magnitudes from figures 7(a) and (b) are compared in figure 8. The complex image method gives good agreement for the effect of plasma inductive coupling for all five modes simultaneously, using only the three parameters listed above which correspond to physically reasonable values of experimental parameters.

5.1. Dependence of mode frequency and impedance amplitude on the plasma density

Figure 9 compares the measurements of (a) mode frequency shift and (b) impedance magnitude, with calculations using the complex image mutual partial inductance model, similarly to figure 8 except that now the dependent variable is the plasma density for a single mode $m = 6$. Again, the agreement between experiment and model is good for both the frequency shift and the impedance magnitude, using the same parameters as for figure 7, namely the pressure, electron density, and plasma distance.

The model results are extrapolated to the limit of low plasma density which corresponds to vacuum. The limit of high plasma density for the calculated values of frequency shift and antenna impedance were compared with experiment by replacing the plasma by a metal plate at the estimated plasma interface distance of 1.2 cm from the antenna. This distance was initially deduced from fitting the impedance spectra for plasma in figure 7. As shown by the low- and high-density asymptotes in figures 9(a) and (b), the values measured respectively in vacuum, or with a metal plate, are reasonably consistent with the complex image model. The measured plasma density increased by one order of magnitude, from $8 \cdot 10^{15}$ m^{-3} to $9 \cdot 10^{16}$ m^{-3} for the RF power range 50–500 W, but as can be seen in figure 9(a), the measured frequency shift never approached that for a perfect screen, because the electron density would have to be unreasonably high for the plasma conductivity to behave as a metal conductor ($\sigma \sim 10^6$ S m^{-1} for stainless steel).

The calculated range of real skin depth in figure 9 was from 6 cm (at 50 W) to 2 cm (at 500 W). 50 W was the lowest power for which the plasma makes the transition to the H-mode, and the associated skin depth is approximately equal to the electrode gap 5.5 cm. For 500 W, the small skin depth means that the power deposition now occurs close to the dielectric surface. Interestingly, there is a minimum in the impedance which corresponds to an optimum power transfer efficiency [5]. This minimum occurs because the vacuum limit (no

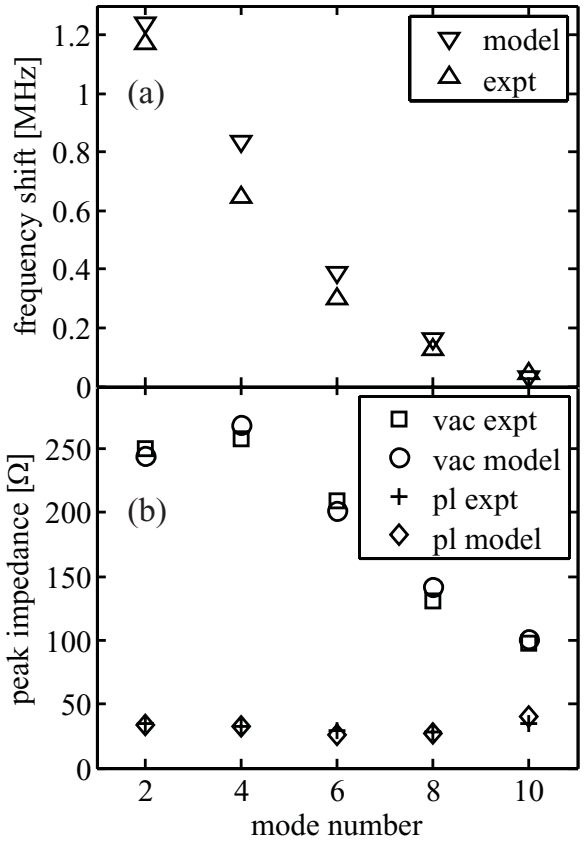

Figure 8. Comparison of model and experimental measurement for (a) the mode frequency shift due to plasma coupling, and (b) the impedance values, at resonance, in vacuum and with plasma. The data are taken from figures 7(a) and (b).

plasma) and the infinite conductivity limit (screen) both imply no dissipation, i.e. no power transfer to a plasma.

6. Conclusions

The complex image method of Part I [1], combined with a matrix solution for the mutual partial inductances, has been used to calculate inductive plasma coupling to a planar resonant network antenna. This model provides a good agreement to the measured antenna impedance frequency spectrum for a range of mode resonances and plasma densities. The complex image method and mutual partial inductance approach can therefore be used to design even complicated structures for planar inductively-coupled plasma sources by accounting for the effect of plasma coupling on the source network.

Acknowledgments

We thank Dr C Hollenstein for many useful comments, and Drs J Larrieu and P Fayet of Tetra Pak SA, Romont, Switzerland, for their advice and support. The development of the plasma source was supported by the Swiss Commission for Technology and Innovation grant no. CTI 14693.1 PFIW-IW.

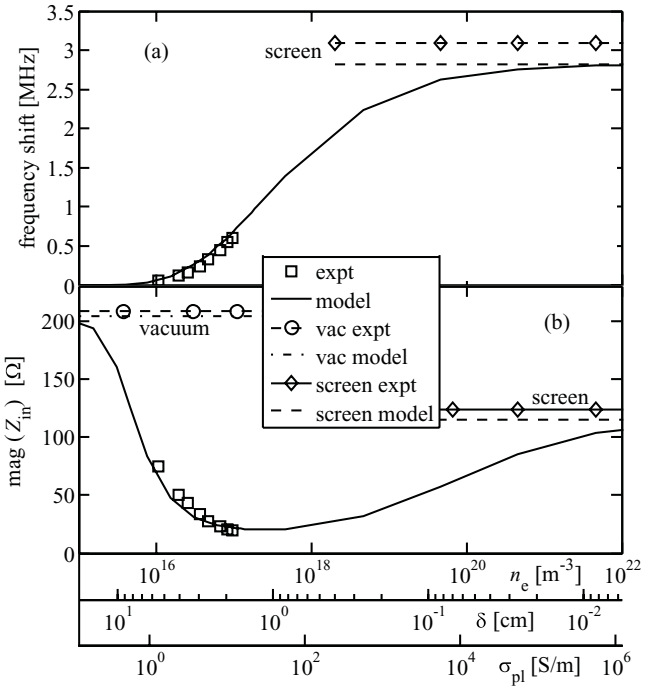

Figure 9. Comparison of model and measurement for (a) the mode frequency shift due to plasma coupling, and (b) the antenna input impedance at mode resonance with plasma. The x-axis is represented in terms of electron density n_e, the real part δ of the plasma skin depth, and the real part of the plasma electrical conductivity σ_{pl} [1]. The measured and calculated asymptotes for the limits of low plasma density (vacuum) and high plasma density (perfectly-conducting screen) are shown by horizontal lines. The input RF powers for the eight experiment points were {50, 80, 100, 150, 200, 300, 400, 500} W, in order of increasing electron density. Mode $m = 6$, argon pressure 1 Pa.

Appendix A. Expressions for mutual partial inductance

General expressions are given by Paul [10] and Grover [12]. Figure A1 shows the simplest geometry which is sufficient to describe all of the mutual partial inductances used in this work. The leg tubes, stringer strips, and their images, are replaced by filaments coincident with their axis. The mutual partial inductance of the filament pair in figure A1 is

$$M = \frac{\mu_0}{4\pi}\left[\alpha \sinh^{-1}\frac{\alpha}{d} - 2\beta \sinh^{-1}\frac{\beta}{d} + s\sinh^{-1}\frac{s}{d} - \sqrt{\alpha^2+d^2} + 2\sqrt{\beta^2+d^2} - \sqrt{s^2+d^2}\right], \quad \text{(A.1)}$$

where $\alpha = 2l + s$, $\beta = l + s$, inductances are in henries, and lengths in meters. This gives a good approximation for separation d much larger than the conductor cross-section width.

Simpler approximations of (A.1) can be found in special cases [10, 12] such as parallel filaments with no offset ($s = -l$ in figure A1), for which the mutual partial inductance is $M \approx \frac{\mu_0}{2\pi} l\,[\ln(l/h) - 1]$, where $2h = d \ll l$. This is the approximation used for parallel wires in Part I [1].

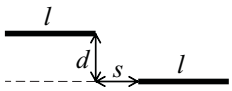

Figure A1. Geometry of parallel, offset filaments of equal length l, distance d apart and offset by s, for calculation of the mutual partial inductances.

Self partial inductance, which is a special case of mutual partial inductance [10, 12], depends on the form of the conductor cross-section: For the cylindrical legs, $L_{\rm leg} \approx \frac{\mu_0}{2\pi} l_{\rm leg}\,[\ln(2l_{\rm leg}/a) - 1]$ as used in Part I [1]; for a stringer strip, $L_{\rm str} \approx \frac{\mu_0}{2\pi} l_{\rm str}\left[\ln(2l_{\rm str}/w) + \frac{1}{2}\right]$ was used [8, 12].

Appendix B. Impedance matrix calculations

With reference to figure 2, the antenna node voltages, leg currents, stringer currents, and source currents are respectively written as column vectors:

$$\vec{A} = \begin{pmatrix} A_1 \\ A_2 \\ \vdots \\ A_N \end{pmatrix}, \quad \vec{I} = \begin{pmatrix} I_1 \\ I_2 \\ \vdots \\ I_N \end{pmatrix}, \quad \vec{J} = \begin{pmatrix} J_1 \\ J_2 \\ \vdots \\ J_N \end{pmatrix}, \quad \vec{S}^J = \begin{pmatrix} S_1^J \\ S_2^J \\ \vdots \\ S_N^J \end{pmatrix}, \tag{B.1}$$

and similarly for node voltages $\vec{B}$, stringer currents $\vec{K}$, and source currents $\vec{S}^K$. For consistent numbering, the stringer currents $\vec{J}$ and $\vec{K}$ are extended to N values by setting very large values for the impedance of the $N^{\rm th}$ stringers, which effectively sets $J_N = 0$ and $K_N = 0$ as required by the boundary conditions.

Current conservation at the network nodes (see figure 2) is:

$$J_n = J_{n-1} + I_n + S_n^J, \tag{B.2}$$

$$K_n = K_{n-1} - I_n + S_n^K, \tag{B.3}$$

where the source currents are included. Introducing the lower shift matrix $\mathbf{U}_L$, which has ones on the subdiagonal and zeroes elsewhere, and writing $\mathbf{U} = \mathbf{1} - \mathbf{U}_L$, current conservation expressed in matrix form becomes:

$$\mathbf{U}\vec{J} = \vec{I} + \vec{S}^J, \tag{B.4}$$

$$\mathbf{U}\vec{K} = -\vec{I} + \vec{S}^K. \tag{B.5}$$

Ohm's law for the legs in matrix form, using (2) and (3) is

$$\vec{B} - \vec{A} = \mathbf{Z}_{\rm leg}\vec{I}, \tag{B.6}$$

where $\mathbf{Z}_{\rm leg} = R\mathbf{1} + \mathrm{j}\omega\mathbf{M}$, using $\mathbf{M}$ for the combined mutual partial inductance matrix for the legs, accounting for image currents in the screen and plasma, so that

$$\mathbf{M} = \begin{pmatrix} L_{\rm leg} & M_{12} & \cdots & M_{1N} \\ M_{21} & L_{\rm leg} & \cdots & M_{2N} \\ \vdots & \vdots & \ddots & \vdots \\ M_{N1} & M_{N2} & \cdots & L_{\rm leg} \end{pmatrix}, \tag{B.7}$$

where $M_{nq} = M_{qn} = M_{nq}^{\rm leg/leg} - M_{nq}^{\rm leg/screen} - M_{nq}^{\rm leg/plasma}$, for $n \neq q$.

Ohm's law for the stringers is more complicated than for the legs because of the contribution from the in-line stringers as well as from the opposing stringers. It can be written as

$$A_n - A_{n+1} = \left(r + \frac{1}{\mathrm{j}\omega C}\right)J_n + \mathrm{j}\omega\sum_{q=1}^{N} M^{\rm line}J_q + \mathrm{j}\omega\sum_{q=1}^{N} M^{\rm opp}K_q, \tag{B.8}$$

$$B_n - B_{n+1} = \left(r + \frac{1}{\mathrm{j}\omega C}\right)K_n + \mathrm{j}\omega\sum_{q=1}^{N} M^{\rm line}K_q + \mathrm{j}\omega\sum_{q=1}^{N} M^{\rm opp}J_q, \tag{B.9}$$

where $M^{\rm line}$ represents the combined mutual partial inductance matrix for the in-line stringers, subtracting the mutual partial inductances for image currents in the screen and plasma, and similarly for $M^{\rm opp}$ regarding the opposing stringers. Recognising that the upper shift matrix is the transposition of the lower shift matrix, Ohm's law in matrix form for the stringers is:

$$\mathbf{U}^T\vec{A} = \left[\left(r + \frac{1}{\mathrm{j}\omega C}\right) + \mathrm{j}\omega\mathbf{M}^{\rm line}\right]\vec{J} + \mathrm{j}\omega\mathbf{M}^{\rm opp}\vec{K}, \tag{B.10}$$

$$\mathbf{U}^T\vec{B} = \left[\left(r + \frac{1}{\mathrm{j}\omega C}\right) + \mathrm{j}\omega\mathbf{M}^{\rm line}\right]\vec{K} + \mathrm{j}\omega\mathbf{M}^{\rm opp}\vec{J}, \tag{B.11}$$

whose difference gives

$$\mathbf{U}^T(\vec{B} - \vec{A}) = \mathbf{Z}_{\rm str}(\vec{K} - \vec{J}), \tag{B.12}$$

where we define a stringer impedance matrix as $\mathbf{Z}_{\rm str} = (r + \frac{1}{\mathrm{j}\omega C})\mathbf{1} + \mathrm{j}\omega(\mathbf{M}^{\rm line} - \mathbf{M}^{\rm opp})$.

We now proceed to solve for the leg current vector $\vec{I}$, first by eliminating the node voltage difference using (B.6) and (B.12) to give

$$\mathbf{U}^T\mathbf{Z}_{\rm leg}\vec{I} = \mathbf{Z}_{\rm str}(\vec{K} - \vec{J}), \tag{B.13}$$

and then using (B.5) minus (B.4) to eliminate the stringer current difference in (B.13), to finally obtain:

$$\vec{I} = (\mathbf{U}\mathbf{Z}_{\rm str}^{-1}\mathbf{U}^T\mathbf{Z}_{\rm leg} + 2\mathbf{1})^{-1}(\vec{S}^K - \vec{S}^J). \tag{B.14}$$

This defines the leg currents in terms of the network impedances and the source currents, which are known for symmetrical connections, or for a single ground connection.

The node voltages are found by adding the two pairs (B.4), (B.5) and (B.10), (B.11), and using (B.6) to give:

$$\vec{A} = \frac{1}{2}\left[(\mathbf{U}^T)^{-1}\mathbf{Z}_{\rm str}\mathbf{U}^{-1}(\vec{S}^K + \vec{S}^J) + \mathbf{Z}_{\rm leg}\vec{I}\right], \tag{B.15}$$

$$\vec{B} = \frac{1}{2}\left[(\mathbf{U}^T)^{-1}\mathbf{Z}_{\rm str}\mathbf{U}^{-1}(\vec{S}^K + \vec{S}^J) - \mathbf{Z}_{\rm leg}\vec{I}\right]. \tag{B.16}$$

The matrices $\mathbf{U}$, $\mathbf{Z}_{\rm leg}$, $\mathbf{Z}_{\rm str}$, and their combinations, are always invertible and give physically-reasonable values for the

antenna currents and voltages. Finally, the antenna input impedance is given by the input voltage divided by the input current at the node where the RF power is connected, when the ground nodes are set to zero voltage, i.e.

$$Z_{\text{in}} = A_{\text{RFnode}}/S^{J}_{\text{RFnode}}, \tag{B.17}$$

which can be compared with measurements.

References

[1] Howling A A, Guittienne P, Jacquier R and Furno I 2015 *Plasma Sources Sci. Technol.* (part 1) **24** 065014

[2] Guittienne P, Lecoultre S, Fayet P, Larrieu J, Howling A A and Hollenstein C 2012 *J. Appl. Phys.* **111** 083305

[3] Lecoultre S, Guittienne P, Howling A A, Fayet P and Hollenstein C 2012 *J. Phys. D: Appl. Phys.* **45** 082001

[4] Guittienne P, Fayet P, Larrieu J, Howling A A and Hollenstein C 2012 *55th Annual SVC (Surface Vacuum Coaters) Technical Conf.* (*28 April–3 May 2012*, *Santa Clara, CA, USA*)

[5] Hollenstein C, Guittienne P and Howling A A 2013 *Plasma Sources Sci. Technol.* **22** 055021

[6] Hollenstein C, Howling A A, Guittienne P and Furno I 2015 *Plasma Phys. Control. Fusion* **57** 014010

[7] Guittienne P, Howling A A and Hollenstein C 2014 *Plasma Sources Sci. Technol.* **23** 015006

[8] Jin J 1998 *Electromagnetic Analysis and Design in Magnetic Resonance Imaging* (Boca Raton, FL: CRC Press)

[9] Advanced Energy Industries Inc. www.advanced-energy.com

[10] Paul C R 2010 *Inductance: Loop and Partial* (New York: Wiley)

[11] Ruehli A E 1972 *IBM J. Res. Dev.* **September 1972** 470

[12] Grover F W 1962 *Inductance Calculations: Working Formulas and Tables* (New York: Dover)

[13] Piejak R B, Godyak V A and Alexandrovich B M 1992 *Plasma Sources Sci. Technol.* **1** 179

[14] Gudmundsson J T and Lieberman M A 1998 *Plasma Sources Sci. Technol.* **7** 83

[15] Lieberman M A and Lichtenberg A J 2005 *Principles of Plasma Discharges and Materials Processing* 2nd edn (New York: Wiley)